Improved Vertical Carrier Transport for Green ill-Nitride LEDs Using (In, Ga)N Alloy Quantum Barriers

Cheyenne LynskyS, ¹, *,t Guillaume Lheureux, ¹,t Bastien Bonef, ¹ Kai Shek Qwah, ¹ Ryan C. White, ¹ Steven P. DenBaars, ¹Shuji NakamuraG>, ¹Yuh-Renn Wu, ² Claude Weisbuch, ¹, ³ and James S. Speck ¹

¹ Materials Department, University of California, Santa Barbara, California 93106, USA

IR>J (Received 17 September 2021; revised 30 March 2022; accepted 20 April 2022; published 31 May 2022)

We report on experimental and simulation-based results using (In, Ga)N alloy quantum barriers in c-plane green light-emitting diode (LED) structures as a means to improve vertical carrier transport and reduce forward voltage (V_p) . Three-dimensional device simulations that include random alloy fluctuations are used to understand carrier behavior in a disordered potential. The simulated current density-voltage (J-V) characteristics and modified electron-hole overlap IFmo, d² indicate that increasing the indium fraction in the (In, Ga)Nquantum barriers leadsto a reduced polarization discontinuity at the interface between the quantum barrier and quantum well, thereby reducing Vp and improving 1Fmoc11². Maps of electron and hole current through the device show a relatively homogenous distribution in the XY plane for structures using GaN quantum barriers; in contrast, preferential pathways for vertical transport are identified in structures with (In, Ga)N barriers as regions of high and low current. A positive correlation between hole(electron) current in thep-side (n-side) barrier and indium fraction reveals that preferential pathways exist in regions of high indium content. Furthermore, a negative correlation between the strain Bzz and indium fraction shows that high indium content regions have reduced strain-induced piezoelectric polarization in the Z direction due to the mechanical constraint of the surrounding lower indium content regions. Experimentally, multiple quantum well green LEDs with (In, Ga)N quantum barriers exhibit lower Vp and blue-shifted wavelengths relative to LEDs with GaN quantum barriers, consistent with simulation data. These results can be used to inform heterostructure design oflow Vp, long-wavelength LEDs and provide important insight into the nature of carrier transport in Ill-nitride alloy materials.

DOI: 10.1103/PhysRevApplied.17.054048

I. INTRODUCTION

Coherently grown [000I] oriented heterostructures consisting of (In, Ga)N quantum wells (QWs) and GaN quantum barriers (QBs) exhibit large internal electric fields due to discontinuities in total polarization at the QW/QB interface. Additionally, random compositional fluctuations in nitrides give rise to large potential energy fluctuations for carriers due to the large differences in band gaps between the constituent compounds, AIN, GaN, and lnN. The spatially varying energy landscape at nanometer-length scales will modify the electrical and optical properties. As a result, alloy disorder strongly impacts carrier localization and transport in light-emitting diode (LED) devices [J-5]. These effects become more pronounced for green

LEDs with nigh indium content (In, Ga)N QWs. It was recently demonstrated experimentally and through threedimensional (3D) simulations based on the localization landscape (LL) theory of disorder that polarization barriers and band offsets at the GaN/(ln, Ga)N (lower OB/OW) interface and sequential filling of QWs contribute to the large excess forward voltage in green III-nitride LEDs [6,7]. In addition to identifying a contributing factor to the low wall-plug efficiency of green LEDs, these findings highlighted the importance of using 3D as opposed to ID simulations to accurately describe carrier transport in LEDs. A natural extension is the investigation of device structures that overcome these barriers to carrier transport in high indium composition QWs. In the work presented here, the impact of InxGal-xN quantum barriers on the electrical properties of green-emitting LEDs is examined experimentally and computationally. Structures incorporating lnxGa1-xN QBs will have a reduced polarization

²Graduate Institute of Photonics and Optoelectronicsand Department of Electrical Engineering, National Taiwan
University, Taipei 10617, Taiwan

³ Laboratoire de Physique de la Matiere Condensee, CNRS, IP Paris, Ecole Polytechnique, 91128 Palaiseau Cedex, France

[•] cheyennelynsky@gmail.com tc.Lynsky and G. Lheureux contributed equally to this work.

discontinuity at the QW/QB interface and will also contribute an additional source of alloy disorder to the active reg10n.

Kuo et al. previously explored the advantages of Ino.1Gao 9N barriers in blue LEDs using APSYS simulations [8]. These authors propose that using (In, Ga)N barriers leads to more uniform electron and hole distribution in a multiple-quantum-well (MQW) structure resulting from the lower polarization discontinuity at the QW/QB interface. With more uniform carrier distribution, Auger recombination and thus efficiency droop are reduced. Experimentally, MQW blue LEDs with (In, Ga)N/(In, Ga)N QWs/QBs were demonstrated to have reduced efficiency droop, forward voltage, and wavelength shift with current compared to LEDs with GaN QBs [9]. Liu et al. also demonstrated that (In, Ga)N barriers led to improved carrier injection into deeper (n-side) QWs as evidenced by relative electroluminescence (EL) intensity of lower green-emitting QWs to a top blue-emitting QW [IO].

Prior experimental reports motivate the use of (In, Ga)N barriers in c-plane green LEDs as a means of improving transport. To date, simulations performed on such structures have not accounted for the impact of alloy disorder in the (In,Ga)N barriers. Because compositional alloy fluctuations are a natural consequence of solid solutions and cannot be independently controlled in experiments, simulations present an attractive option for studying their impact on device performance. To understand carrier behavior in a disordered potential, full 3D treatment of the system is required. For this, we turn to a computational approach based on the LL theory of disorder to perform efficient 3D device simulations [11-14]. To simulate the electrical behavior of nitride-based devices, a Poisson-Schrodinger drift-diffusion solver should be used to solve the coupled equations self-consistently. To account for disorderinduced quantum effects, the Schrodinger equation should be solved in 3D for a disordered potential. However, selfconsistently solving for the eigenstates in an alloy system using quantum mechanical calculations is too computationally demanding to be practical [14]. As an alternate approach, the LL model pioneered by Filoche and Mayboroda to obtain an equivalent semiclassical confining potential is applied here [I1-13].

We present here an experimental and simulation-based study on the use of InxGa1-xN quantum barriers in greenemitting III-nitride LEDs. Experimentally, we compare Ino_04Gao.96N and GaN barriers on forward voltage in one-, three-, and five-QW green LEDs and perform characterization using atom probe tomography (APT). One- and two-QW LED structures with InxGa1-xN barriers (where x=0--0.05) are simulated using 3D solver. From 3D simulations, we analyze the electrical device properties and the modified electron-hole overlap. Most importantly, we use simulation data to understand the role ofrandom alloy fluctuations on carrier transport. The results presented here provide valuable, and to our knowledge previously unidentified, information regarding electron and hole transport through lnxGa1-xN alloy quantum barriers in an LED active region. In particular, we identify preferred current pathways through regions with high indium concentration originating from alloy disorder.

II. METHODS

To experimentally study the effect of alloy quantum barriers, green LEDs are grown by atmospheric pressure metalorganic chemical vapor deposition (MOCVD) on (000 I) patterned sapphire substrates with either GaN or lno 04Gao.96N QBs and varying number of QWs. A lowtemperature GaN nucleation layer is followed by 3 µm of unintentionally doped GaN, 2 µm of n-GaN, and a 45-period n-type (ln, Ga)N/GaN superlattice. The active region is undoped and consists of 3-nm (ln, Ga)N QWs, 2-nm Alo 04Gao 96N capping layers, and 8-nm GaN or lno 04Gao.96N QBs. Including (Al, Ga)N capping layers after the QW growth typically enables more aggressive GaN QB growth conditions, such as H2 flow and high temperatures [15-18]. In the structures presented here, which use (ln, Ga)N QBs, such aggressive growth conditions cannot be used as they prevent efficient indium incorporation. Nevertheless, (Al, Ga)N capping layers are standard in Jong-wavelength LED growth and are therefore included in the experimental structures. High resolution xray diffraction w-20 measurements of a thick (In, Ga)N calibration sample are performed on a Panalytical MRD PRO using Cu Ka₁ radiation (A= 1.5405 Å) to calibrate the (In, Ga)N QB growth rate and composition. The LED active region has either one, three, or five QW periods. The p-side of the LED contains JO nm ofp+-GaN, 130nm of p-GaN, and a I0-nm p+-GaN contact layer. A postgrowth anneal in N2/02 at 600°C for 15 min is used to activate the Mg-doped layers. LEDs are fabricated using standard mesa isolation and contact deposition. Pd/ Au is used as the p-contact to GaN to allow for reliable voltage determination. APT measurements are performed on all samples to investigate the LED active region layer thicknesses and compositions. APT sample preparation, evaporation, and reconstruction details can be found in Ref [19].

The c-plane green LED structure presented in Fig. I(a) is used for the simulations. The single-QW structure consists of a 40-nm thick n-GaN layer (donor concentration $Nv = 5 \times 10^{18}$ cm⁻³), a 3-nm lno.22Gao.1&N QW, 7-nm lnxGa1-xN QBs on either side of the QW, and a 50-nm thick *p-GaN* layer (acceptor concentration $NA = 2 \times 10^{19}$ cm⁻³). The indium fraction x in the (In, Ga)N QB is varied from 0 to 0.05. The two-QW structure is identical to the one-QW structure, but an additional QW and QB are added to the active region. (Al,Ga)N capping layers are not used in these simulation structures. The (Al,Ga)N layers incorporated into the

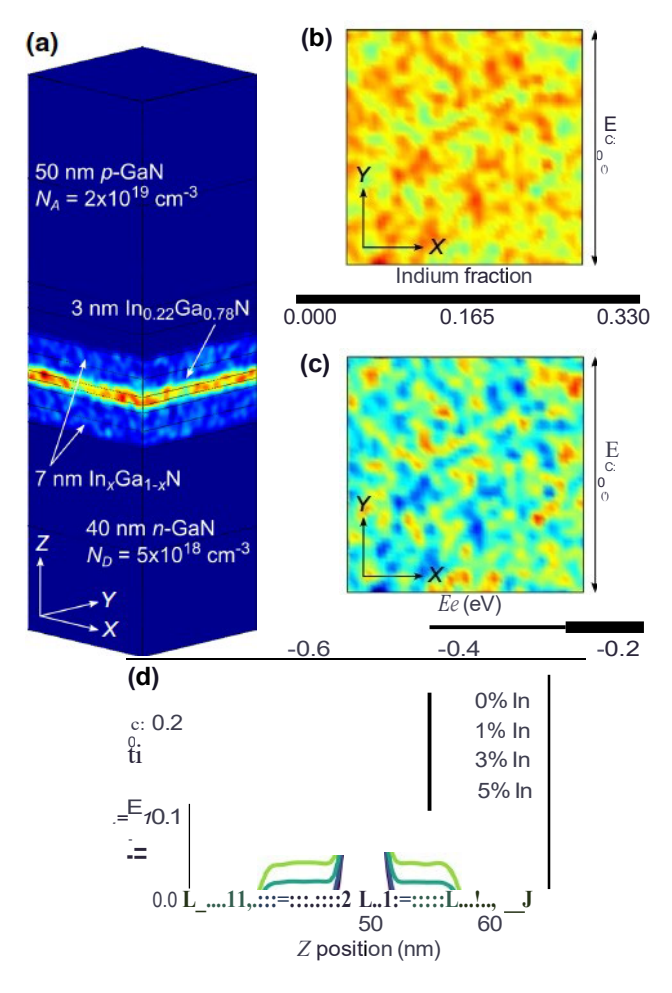


FIG. 1. (a) Full single-QW structure used in the simulations, where the color scale bar is given in (b). (b) XY map of indium distribution in the (ln,Ga)N QW showing random lateral alloy fluctuations. (c) XY map of the conduction band potential Ec(r) in the QW at a bias of 2.9 V. This map is the result of the compositional fluctuations in Fig. 1(b) and the associated variations in band gap, electric field, and carrier injection. (d) Indium alloy composition averaged in the XY plane along the Z direction for the foursimulated structures with 22% indium in the QW and $x^{3/4}$ indium in the QBs, wherex=0, 1, 3,or 5.

experimentally grown samples are thin and contain a low aluminum fraction, as measured by APT. These layers are therefore not expected to strongly impact transport and are excluded from the simulations to avoid uncertainty in defining the complex (In, Ga)N/(AI,Ga)N/(In, Ga)N alloy profiles. Input parameters for each layer in the structure are provided in Table I. The LED structures are meshed using GMSHTM [20,21]. A constant mesh size of 0.6 nm is used in the XY planes and a variable mesh size is used in the Z direction, ranging from I nm in the p-GaN and n-GaN to 0. I nm in the QWs and at the layer boundaries.

The indium alloy composition averaged in the XY plane along the Z direction is shown in Fig. I(d) for all (ln, Ga)N

TABLE I. Simulation parameters used for each layer in the structure.

		(ln,Ga)	(ln,Ga)N	
	n-GaN	NQW	QB	p-GaN
Thickness (nm)	40	3	7	50
Doping (cm- ³)	5×10^{18}	1×10^{17}	1×10^{17}	2×10^{19}
Ea (meV)	25			170
$\mu e (\text{cm}^2/\text{Vs})$	200	300	300	32
$\mu h \text{ (cm}^2/\text{Vs)}$	23	10	10	5
< n (s)	10	1×10^{-7}	1×10^{-7}	6 x 10-IO
'P (s)	7 x 10-IO	1×10^{-7}	1×10^{-7}	10
$Bo (cm^3/s)$	2x 10-II	2×10 -II	2 x 10-II	$2x10^{-11}$
Co (cm ⁶ /s)	6 x 10-JI	6×10^{-31}	6×10^{-31}	6 х 10-Л

OB compositions used in the simulations. The composition profiles are based on those observed experimentally by APT [1,22]. In the 3D computations, the average indium composition of a layer is first defined, and a random number generator is used to assign indium and gallium atoms to each cation lattice site. The Gaussian averaging method described extensively in Ref. [14] is used to realize a continuous fluctuating composition. Figure I(b) shows the random alloy map generated; the XY slice in the QW exhibits random alloy fluctuations as evidenced by the In-rich and In-poor regions. Although there are alloy fluctuations, the local band gap Eg is retained. The local alloy composition is used to assign the band gap Eg, dielectric constant E_r and effective mass m^* at each mesh node. The values of these parameters can be found in Table I of Ref. [14]. For an InxGa1-xN alloy with indium fraction x, these parameters are determined by interpolating between GaN and InN according to the following equations

$$E_g^{\ln_x \text{Ga}_{1-x} \text{N}} = (1-x)E_g^{\text{GaN}} + xE_g^{\text{InN}} - 1.4x(1-x), (1)$$

$$\epsilon_r^{\text{In}_x\text{Ga}_{1-x}\text{N}} = (1-x)\epsilon_r^{\text{GaN}} + x\epsilon_r^{\text{InN}}, \tag{2}$$

$$m^{*, \text{In}_x \text{Ga}_{1-x} \text{N}} = [(1-x)/m^{*, \text{GaN}} + xm^{*, \text{InN}}]^{-1}.$$
 (3)

The XY map of the conduction band potential Ec(r) in the QW is shown in Fig. I(c), where the conduction band offsets between GaN and (In, Ga)N are taken to be 63% of the band gap difference. However, the energy levels of electrons and holes are not given by the conduction and valence band potentials Ec, v(r) as quantum effects occur due to the size and lateral dimensions of energy fluctuations. In the effective mass approximation, the true carrier energy levels are obtained by solving the Schrodinger equation obeyed by carriers in the fluctuating potential [14].

The 3D drift-diffusion charge control (3D DDCC) solver is employed here to perform device simulations [23,24]. In this model, the Schrodinger eigenvalue equation [Eq. (4)]

is replaced with the landscape equation [Eq. (5)]

$$Hi\{!(r) = Ei\{!(r), \tag{4}$$

$$Hue, h(r) = 1, (5)$$

where the Hamiltonian for electrons and holes is given by

$$\hat{H} = -\frac{\hbar^2}{2m_{eh}^*} \Delta + E_{c,v}(\mathbf{r}), \tag{6}$$

and i/1 is the wave function, E is the eigenenergy, ue,h(r) are the electron and hole landscape functions, $m!_h$ are the electron and hole effective masses, and Ec,v() are the conduction and valence band potential energies. The semiclassical effective potentials 1/ue,h(r) from LL theory capture quantum mechanical effects, such as carrier confinement [13]. By replacing an eigenvalue problem with a Dirichlet problem, self-consistently solving the coupled Poisson-landscape drift-diffusion equations becomes computationally tractable using the 3D DDCC solver [14].

Coherently grown III-N heterostructures in the [000l] orientation exhibit large internal electric fields resulting from discontinuities in spontaneous and piezoelectric polarization that must be accounted for in device simulations. A 3D continuum stress-strain model is solved using the finite element method to calculate the strain distribution. From the strain distribution, the strain-induced piezoelectric polarization pP2can be evaluated by

$$\mathbf{P}^{pz} = [\mathbf{e}] \cdot [\varepsilon] = \begin{bmatrix} e_{15}\varepsilon_{xz} \\ e_{15}\varepsilon_{yz} \\ e_{31}(\varepsilon_{xx} + \varepsilon_{yy}) + e_{33}\varepsilon_{zz} \end{bmatrix}, \quad (7)$$

where £xx, syy, czz are normal strains and cxy, syz, czx are shear strains. e15, e31, e33 are the piezoelectric coefficients (Table II) from the piezoelectric tensor, where the other tensor terms are zero due to the 6mm point symmetry for the wurtzite crystal structure. The spontaneous polarization J>"P values, as related to the GaN buffer layer, are calculated from

$$J > "P = ax + b(1 - x) + cx(1 - x),$$
 (8)

where a, b, and c are coefficients given in Table II and x is the alloy composition of lnxGa1-xN or AlxGa1-xN. Taking the divergence of the total polarization $P^{10131}(r)$ over the entire domain, where ptotal(r) = ppz + psP, gives the induced fixed polarization charge Ppoi(r)

V.
$$ptotal(r) = Ppot(r)$$
. (9)

The polarization-induced charge Ppot(r) is solved once outside the self-consistency loop and is input into the Poisson equation to calculate the electrostatic potential < p(r)

TABLE II. Piezoelectric polarization coefficients for GaN, lnN, and AIN and spontaneous polarization coefficients for (In,Ga)N and (Al,Ga)N alloys [25--27].

Piezoelectric	e15 (C cm- ²)	e31 ($C \text{ cm}^{-2}$)	e33 ($C cm^{-2}$)
GaN	-0.40	-0.49	0.73
InN	-0.40	-0.49	0.73
AJN	-0.48	-0.58	1.55
Spontaneous	a (C cm-2)	b (C cm-2)	c (C cm-2)
(In,Ga)N alloy (Al, Ga)N alloy	-0.042 -0.090	-0.034 -0.034	0.037 0.021

and then Ec, v(r). The electron and hole densities, n and p, respectively, are initially guessed. The Poisson equation is given by

$$\nabla \cdot (\varepsilon \nabla \varphi(\mathbf{r})) = e(n - p + N_A^- - N_D^+ \pm \rho_{\text{pol}}(\mathbf{r})), \quad (10)$$

where s is the dielectric permittivity, e is the electron charge, and NA- and N'jj are the ionized acceptor and donor densities. After obtaining Ec, v(r), the landscape equation [Eq. (5)] is solved for the landscape functions ue, h(r). The effective potentials 1/ue, h(r) determine the bottom energy for the local density of states (LOOS, p) of the disordered system, which in landscape theory can be computed from Weyl's law in 3D [Eq. (11)] [13]. The carrier densities are then calculated from Eqs. (12) and (13)

$$\rho_{3D}(E, \mathbf{r}) = \frac{\sqrt{2}m_{e,h}^*}{\pi^2 \hbar^3} \sqrt{|E - 1/u_{e,h}(\mathbf{r})|}, \tag{11}$$

$$n(E,\mathbf{r}) = l + O_{\mathbf{r}}O_{\mathbf{o}}(E, r)fn(E)dE,$$
(12)

$$p(E, \mathbf{r}) = -00 \ p30(E, \mathbf{r})f_{*,*}(E)dE_{*,*}$$
 (13)

where fn(E) and $f_{,,}(E)$ are the Fermi-Dirac distributions for electrons and holes, respectively. The carrier densities are input into the drift-diffusion [Eqs. (14) and (15)] and recombination [Eqs. (16) and (17)] equations, which are given by the following

$$Jn = n\mu, nVEFn,$$
 (14)

$$JP = PJJ, pVEFp,$$
 (15)

$$\vee \cdot (Jn,p) = \pm e[Ao + Bonp + Co(n^2p + np^2)], \tag{16}$$

 J_n and J_P are the electron and hole current densities, $J_{l,n}$ and $J_{l,p}$ are the electron and hole mobilities, and EF and EFP are the quasi-Fermi levels of electrons and holes. The

Shockley-Read-Hall (SRH) model is used to account for nonradiative recombination due to defects through the rate Ao [Eq. (17)]. rn and rp are the nonradiative electron and hole lifetimes, n; is the intrinsic carrier density, E; is the intrinsic energy level, and E_l is the trap energy level, which is assumed to be at midgap. ks is the Boltzmann constant and Tis taken at room temperature. Bo and Co are the radiative and Auger nonradiative recombination coefficients, respectively, of bulk materials without disorder or electric field (see Ref. [14] for a more complete discussion). In the computation, the electron-hole overlap is captured by locally calculating n(r) and p(r) [Eqs. (12) and (13)] and thus all recombination rates [Eqs. (16) and (17)].

In the simulation process, the spatial dependence of the total polarization $P^{10131}(\mathbf{r})$ is first calculated to obtain the fixed polarization charge Ppo1(r). Next, the Poisson equation is solved for the electrostatic potential </>(r) which is used to calculate Ec(r) and Ev(r). The landscape equations Hue(r) = 1 and Huh(r) = 1 are then solved for ue(r) and uh(r). From the effective potentials 1/ue(r) and 1/uh(r), the carrier densities of electrons and holes are calculated and fed back into the Poisson-drift-diffusion equations to be solved in a self-consistent manner. Convergence is achieved when the potential energy difference between two consecutive iterations is less than 10^{-5} eV.

III. RESULTS & DISCUSSION

A. J-V characteristics

Current density versus voltage (J-V) curves obtained from 3D DDCC simulations of the single-QW structure are plotted in Fig. 2(a) to explore the effect of (In, Ga)N QBs on forward voltage VF. As the indium composition in the QBs is increased from 0% to 5%, VF systematically decreases. At 35 A cm⁻², the voltage decrease is 0.05 V per one percent indium in the QB. The same curves for the two-QW structures with varying QB indium composition are shown in Fig. 2(b). Again, a decrease in voltage occurs with increasing indium fraction of the QB. For a given indium content, the two-QW structures exhibit higher forward voltage compared to the one-QW structures. This result agrees with prior experimental and simulation studies that show that for planar LEDs without engineered V-defects, additional OWs with undoped barriers are accompanied by a voltage penalty [6,7]. The source of the voltage penalty is assigned to polarization barriers and conduction band offsets at the QB/QW interface and sequential filling of QWs. Because the simulated structures used here are planar and do not contain a high density of V-defects, a voltage penalty with increasing QW number is expected.

While overall the two-QW structures present higher VF than the one-QW structures, the decrease in VF with increasing QB indium composition is also more significant. Here the voltage decrease per one percent indium in

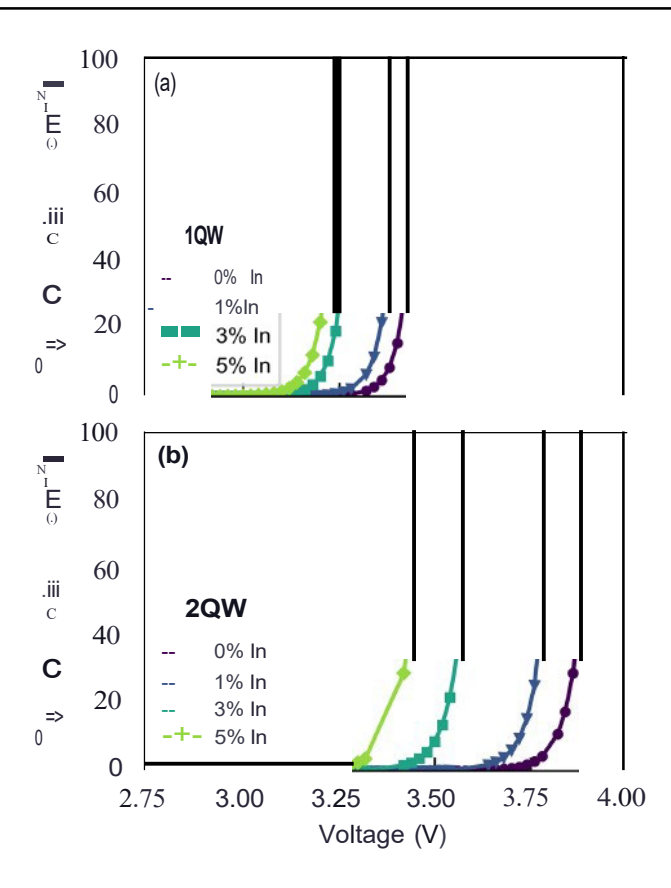


FIG. 2. *J-V* curves from 3D simulations of green LED structures with lnxGa1-xN quantum barriers of varying indium composition and either (a) one QW or (b) two QWs.

the QB is 0.11 Vat 35 A cm-². The advantage of (In, Ga)N alloy QBs on electrical properties is therefore cumulative with increasing QW number. By increasing the indium fraction in the QB, the barrier to transport associated with each QW is decreased. For the 0% indium QB case, the voltage penalty for going from one to two QWs is 0.45 V; in contrast, the voltage penalty is only 0.22 V for the 5% indium QB structures. These results may be significant for commercial LEDs where large numbers of QWs are frequently used to improve the optical efficiency of LEDs but come with the drawback of worse electrical efficiency. (In, Ga)N QBs may provide a path to reduce the voltage penalty associated with increasing number of QWs.

B. Carrier recombination

Simulations can also be used to assess the role of (In, Ga)N QBs on electron-hole recombination and hence provide additional insight into the reduction in VF. Equation (16) shows the relationship between the recombination rates and current density. In the 3D DDCC simulations, n(r) and p(r) are computed in 3D for all r to calculate the SRH, radiative, and Auger recombination rates. Thus, the overlap of the carrier density is captured in the calculated n and p in the simulations. For a fixed

QW thickness and crystallographic orientation, an increase in wave function overlap in the Z direction at a given current density implies a reduced net electric field in the QW layer due to the flattening of the conduction and valence bands. Evaluating the electron-hole wave function overlap is therefore one way to assess recombination and electric fields in the QW.

Because the landscape equation is used here instead of the Schrodinger equation, the eigenvalues and eigenstates are not directly calculated. Instead, the carrier densities obtained in 3D are determined from the p assuming Weyl's law [Eqs. (11}--(13)] [13]. The normalized carrier densities for electrons and holes are calculated as follows:

$$nuorm (x,y,z) = rx2 rY2 J,22 \begin{pmatrix} \\ \\ Jxi Jy, \\ 21 n x,y,z \end{pmatrix} dxd d \qquad (18a)$$

$$Puorm(x,y,z) = \frac{p(x,y,z)}{\underset{J \neq 1}{rx2} \underset{J \neq 1}{rn} \underset{z \mid p}{J,22} \underset{y}{(x z)} \underset{y}{dxd} \underset{y}{dz'}} (18b)$$

$$\int_{XJ} \frac{x^2 Y b Z^2}{P norm(x,y,z)} dx dy dz = 1.$$
 (19b)

The normalized densities are computed over the entire XY simulation domain. For the single-QW structure investigated here, Z1 is chosen to be the middle of the n-side quantum barrier (Z1=45 nm) and Z2 to be the middle of the p-side quantum barrier ($Z_2 = 55$ nm). By defining the domain boundaries in this way, the carrier densities in the quantum barriers are considered, representing the wave function penetration in the barriers, which is largely increased due to compositional fluctuations. Normalization allows nuorm(x,y,z) and Pnorm(x,y,z) to be treated as the probability of electron and hole presence in the Z1 to Z2 domain. $n_{00}rm(x,y,z)$ and Pnorm(x,y,z) are then used to define the modified electron-hole overlap IFmo, d², a proxy for the square of the electron and hole wave function overlap 1Fehi2, where

$$|\text{Fmoc}||^2 = 1 \frac{x2! Y2122}{Jnnorm(x,y,z)}$$

$$\frac{JPnorm(x,y,z)}{Jnnorm(x,y,z)} dxdydzl^2$$
(20)

1Fmoc11² as a function of current density for the single-QW LED structure with different QB indium compositions is given in Fig. 3(a). 1n all cases, 1Fmocll increases with current density due to progressive carrier injection into the QW and subsequent reduction of the quantum confined Stark effect (QCSE) by partial screening of the

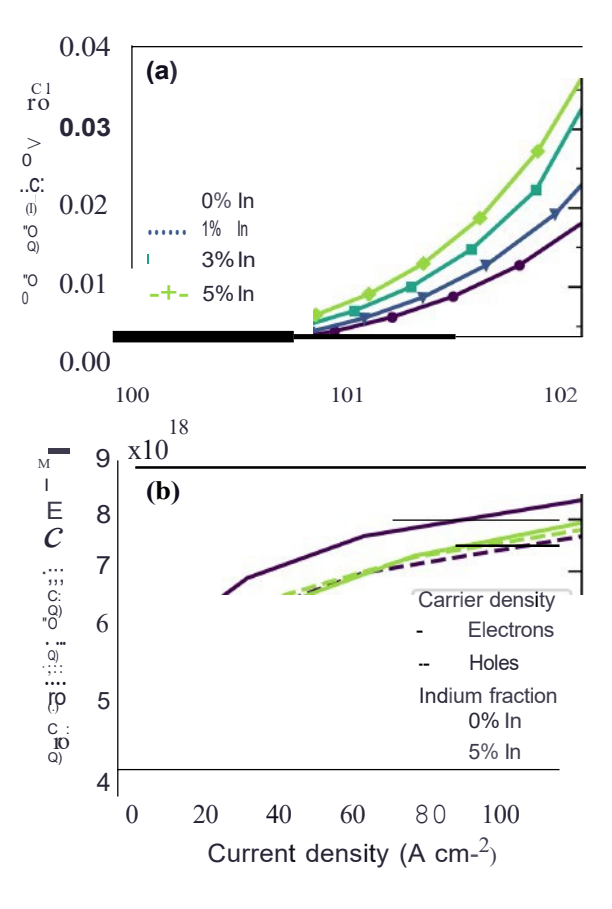


FIG. 3. Simulated dependence of (a) the modified electronhole overlap JFnxxd² and (b) mean electron (solid) and hole (dashed) carrier density on current density for single-QW LEDs with different (In,Ga)N barrier compositions.

electric field. For a given current density, 1Fmoc11² increases with increasing QB indium composition. This trend is attributed to a decrease in the net electric field in the QW resulting from the reduced polarization discontinuity at the QW/QB interface and reduced band offsets when using (In, Ga)N barriers as opposed to GaN barriers. With InN and GaN having similar spontaneous polarization coefficients but large lattice mismatch, the spontaneous polarization-induced electric field in the QW is small relative to the electric field arising from piezoelectric polarization.

Increasing 1Fmoc11², and thus the recombination rate in the QWs, should also lead to a decrease in the steadystate carrier density at a given current density according to Eq. (16). To explore this, the mean electron and hole densities in the single-QW structure are computed according toEq.(21),

$$\frac{J^{2} J, Y^{2} fz 2^{2} n(x,y,z) dxdydz}{n(x,y,z) dxdydz}$$

$$\frac{J}{n(x,y,z)} = \frac{J^{2} J_{y} fz 2^{2} n(x,y,z) dxdydz}{Z^{2} J_{y} fz 2^{2} p(x,y,z) dxdydz}$$

$$\frac{J^{2} J_{y} fz 2^{2} n(x,y,z) dxdydz}{Z^{2} J_{y} fz 2^{2} p(x,y,z) dxdydz}$$

$$\frac{J^{2} J_{y} fz 2^{2} n(x,y,z) dxdydz}{Z^{2} J_{y} fz 2^{2} p(x,y,z) dxdydz}$$
(21a)

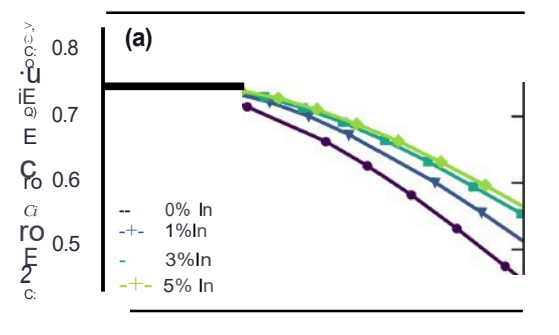
$$p(x,y,z) = \int_{1}^{x} x^{2} \int_{1}^{y} Y^{2} J_{z}^{2} 2p \left(x,y,z\right) dx d_{y} d_{z}$$

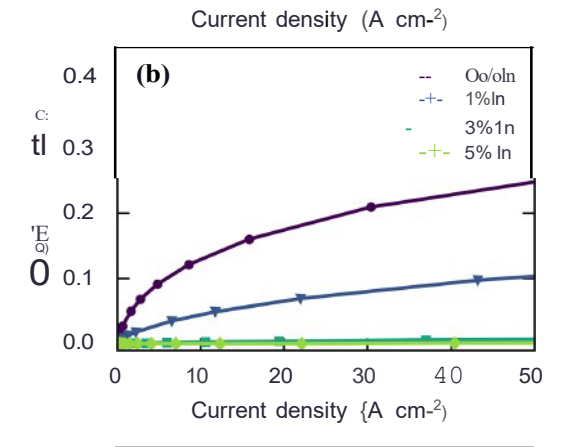
$$Z^{2} - Z^{1}$$
(21b)

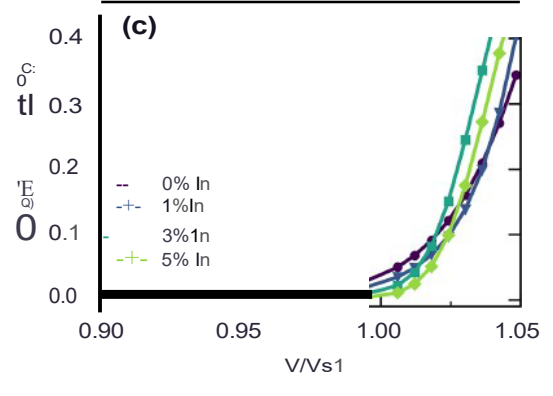
The mean carrier densities are computed in the same domain as the normalized carrier densities. The dependence of ii and p on current density for structures with different QB indium fraction are plotted in Fig. 3(b). In all cases, the mean carrier density increases sublinearly with injection current as n scales approximately between $J^{1/2}$ and $J^{1/2}$, following Eq. (16). As the indium fraction in the QB is increased, there is a very small change in p but a decrease in p ii. With higher indium fraction in the QB, IFmool² is increased [Fig. 3(a)] leading to faster recombination and reduced total carrier density [Fig. 3(b)].

A change in IFmool² is expected to impact the dependence of internal quantum efficiency (IQE) on current density, where the IQE is defined as the ratio of the radiative recombination rate to the recombination rate due to all processes. Figure 4(a) shows the IQE curves for single-QW structures. While the peak IQE is similar for all structures, with higher QB indium fraction a slight increase in the current density at peak IQE and a significant reduction in droop are observed. The improvement in droop behavior can be explained by the lower steady-state carrier density and therefore reduced Auger rate $(Co(n^2p + np^2))$ relative to the radiative rate (Bonp). An additional impact on carrier recombination is seen when looking at the fraction of current due to carrier overflow from the QW at higher currents, computed as the difference between the injected current and the recombination currents. It is shown in Fig. 4(b) that at a given current density, the overflow fraction of current is smaller for structures with higher indium fraction in the barrier and that overflow becomes negligible for LEDs with 3% and 5% indium. This trend can be better understood by plotting the dependence of

overflow fraction on the ratio of the applied voltage V to the built-in GaN p-n diode voltage VBI ($V_{81}=3.3$ V) with ND= 5 x 10^{18} cm-3 and NA= 2 x 10^{19} cm-3 (assuming I% acceptor ionization). These results are shown in Fig. 4(c) where the curves for different QB indium fractions closely overlay one another. From the data in Figs. 4(b) and 4(c), it is observed that the overflow current is a result of applying a bias in excess of VBI. This emphasizes that carrier overflow becomes significant only when V exceeds VBI of the GaN p-n junction and that overflow is not connected to the tum-on voltage of the LED. Therefore, incorporating (In, Ga)N QBs in green LED structures not only reduces the forward voltage but also leads to lower carrier overflow. To further avoid overflow current at high diode voltages, an (Al, Ga)N electron blocking layer should be used. In Fig. 4(d), the dependence of the Auger fraction of current on V/VBI is shown. Unlike overflow, there is an appreciable fraction of Auger at V/VBI < I, a regime where droop is observed in Fig. 4(a). The Auger fraction then begins to decrease with increasing Vf VBI as a smaller fraction of carriers are injected in the QW, corresponding to the increase in carrier overflow. At V/VBI = 1.05, overflow and Auger have approximately







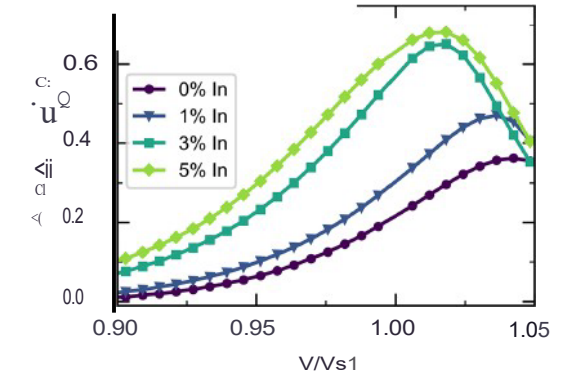


FIG. 4. Simulated dependence of (a) internal quantum efficiency (IQE) at low current densities and (b) overflow fraction of current density for single-QW LED structures. (c) Overflow fraction dependence on the ratio of applied voltage V to built-in diode voltage VBI, where VBI = 3.3 V. (d) Auger fraction dependence on V/VBI.

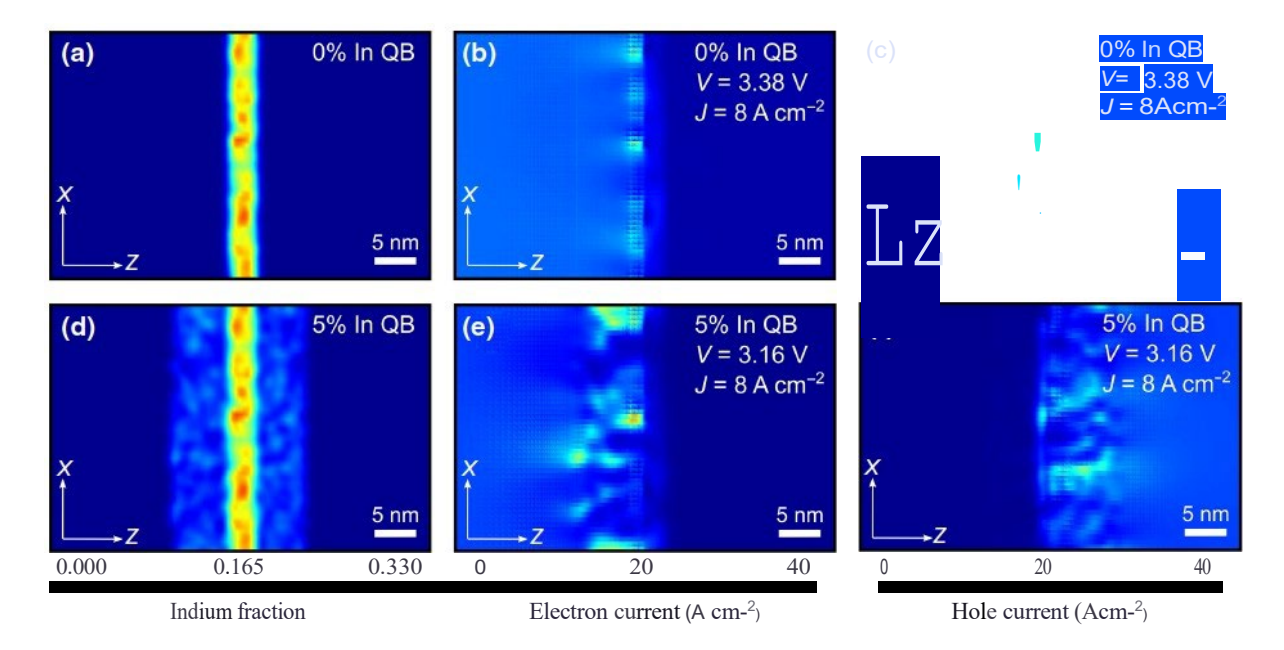


FIG. 5. The XZ plane (a) indium composition map,(b) electron current density map, and (c) hole current density map for a one-QW LED with 0% indium barriers. The XZ plane(d) indium composition map, (e) electron current density map, and (f) hole current density map for a one-QW LED with 5% indium barriers. It can be seen that the high indium composition quantum barrier structure results in high electron and hole current pathways.

the same contribution to the total current and therefore to droop.

C. Percolative pathways

3D simulations allow for the determination of the percolative transport paths in Ill-nitride materials that arise due to random alloy fluctuations. Comparing structures with GaN and (In, Ga)N barriers, spatial differences in electron current can be visualized. Figure 5 shows indium, electron current, and hole current maps in the XZ plane for one-QW structures with either GaN or Ino.osGao 95N quantum barriers. The (In, Ga)N compos1tton maps for the GaN and Ino.osGao_95N QB structures are shown in Figs. 5(a) and 5(d), respectively. At a current density of 8 A cm-², high electron current [Fig. 5(e)] and hole current [Fig. 5(f)] pathways are observed for the structure with (In, Ga)N barriers. In contrast, the electron current [Fig. 5(b)] and hole current [Fig. 5(c)] are more homogenous for the GaN QB structure and do not show the same regions of extreme high and low current. The inhomogeneous current maps indicate a secondary effect of (In, Ga)N barriers in addition to the average reduced polarization discontinuity at the QW/QB interface. From the current maps

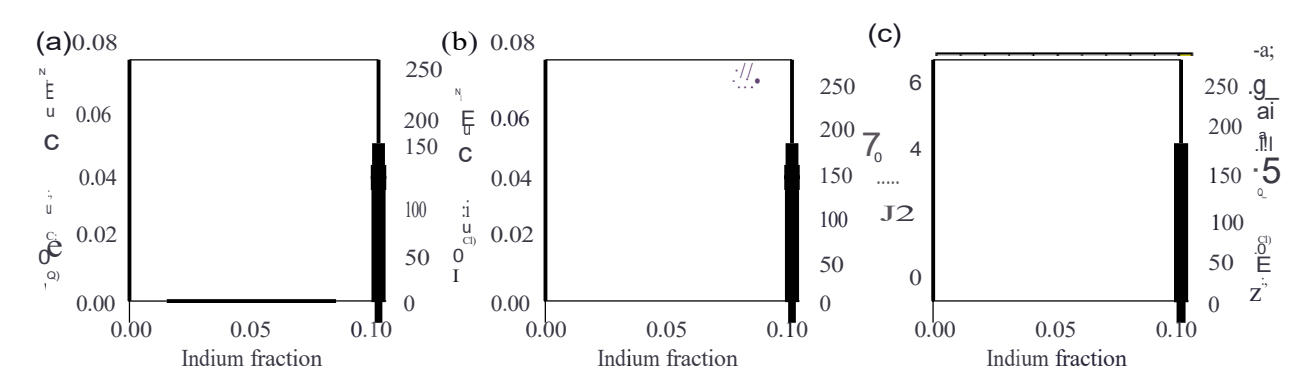


FIG. 6. Correlation plots for the one-QW LED structure with 5% indium barriers (a) Electron current density IJnI as a function of the indium composition in then-side QB and (b) hole current density IJPI as a function of the indium composition in the p-side QBat V=2.9 V, below VB1- Both the electron and hole current densities are higher in regions of high indium composition. (c) Z component normal strain szz as a function of indium composition. Bzz decreases with indium composition in the QB.

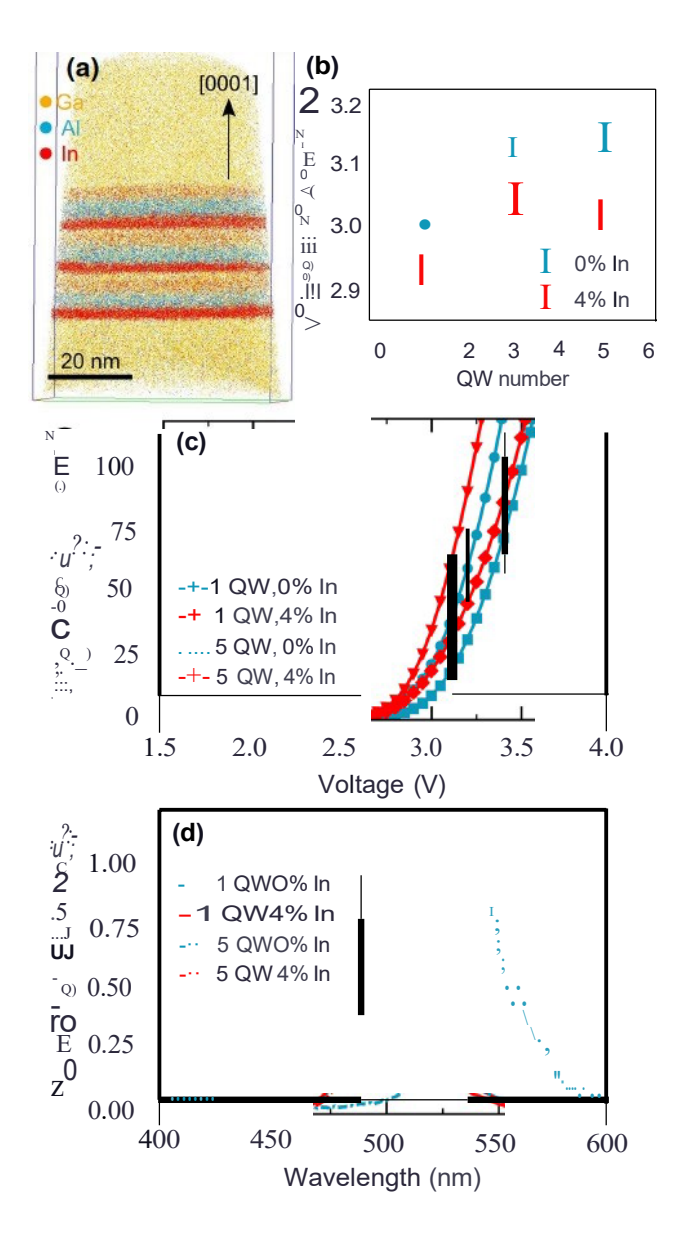


FIG. 7. (a) Atom probe tomography 3D reconstruction of the active region of a three-QW LED with 4% indium (In,Ga)N quantum barriers. (b) Experimental *Vp* measured at 20 A cm⁻² for LEDs with one, three, or five QWs and either 0% or 4% indium (In, Ga)N QBs. A reduction in *Vp* is measured for LED structures with (In,Ga)N quantum barriers. (c) *J-V* curves and (d) electroluminescence (EL) spectra for LEDs with one or five QWs and 0% or 4% indium (In,Ga)N quantum barriers.

it is clear that there are preferential paths for carriers to flow through the barrier layers to then inject the QW. Alloy disorder, introduced through the addition of indium to the QB, is a likely explanation for the spatial variation in current through the structure. It is then of interest to identify what nanoscale variations in materials properties lead to the altered carrier transport.

To further explore the role of alloy fluctuations and percolative pathways on carrier transport, the magnitude of electron current |Jn| in the n-side QB and the magnitude of hole current IJP in the p-side QB are plotted as a function of indium composition in Figs. 6(a) and 6(b), respectively, for each computational node in the QBs. We note here that scatter plots obtained using IJn and IJP are nearly identical to those using Jnz and Jpz, respectively. For both the n-side and p-side QBs, nodes are taken in the full 30 nm x 30 nm XY plane. The n-side QB domain is defined from Z = 41 to Z = 47 nm for a total number of 150 858 nodes and the p-side QB domain is defined from Z = 52 to Z = 57 nm for a total of 124 828 nodes. The scatter plots in Fig. 6 show the properties associated with each simulation node in the given domain. Here, the average indium fraction of the QB is fixed at 0.05 and the variations from approximately 0.02 to 0.08 represent the random alloy fluctuations for a simulation node. A positive correlation is observed between electron current in the n-side barrier and indium fraction as well as hole current in the p-side barrier and indium fraction. This correlation indicates that the favorable path for carriers to transport through (In, Ga)N quantum barriers is along the regions of high indium content. This can in part be understood by considering the reduced conduction and valence band offsets in regions of high QB indium composition. However, another factor that should also be examined is the effect of alloy composition on strain, and therefore strain-induced piezoelectric polarization ppz

A scatter plot of the dependence of the Z-component normal strain ezz on indium composition in the quantum barrier is given in Fig. 6(c). The domain shown is for the p-side QB from Z = 52 to Z = 57 nm; however, similar results are obtained for the n-side QB. The average ezz is approximately 3 x 10⁻³ and a negative correlation is observed where ezz decreases with increasing indium fraction in the p-side QB. At first this result may seem counterintuitive; typically for a uniform alloy, a larger ezz would be expected for a higher indium composition (In, Ga)N film strained to an underlying GaN lattice. However, a random alloy (ln, Ga)N film with regions of high and low indium composition is being considered here. The regions of high indium composition will exhibit a smaller ezz as the lattice is constrained in the Z direction by the surrounding low indium composition regions. Conversely, the low indium compositions will have a larger ezz due to the surrounding regions of high indium composition. A correlation plot of ezz as a function of indium fraction for the one-OW structure with I\% indium OBs (not shown here) gives the same negative correlation; however, the average ezz is less than the average ezz for the 5% indium QB structure, which is qualitatively the expected trend. The negative correlation between ezz and indium fraction in the OB, for a structure with a fixed average indium fraction, indicates that areas of higher indium content have a relatively lower Z component of pPz. The high indium composition, low ppz, regions may further provide

favorable, low barrier pathways for carriers to transport through the QBs and into the QWs. This agrees with previous results showing that polarization discontinuities at the QW/QB interface result in a polarization barrier for carrier transport and thus excess voltage in green LEDs [7].

D. Experimental measurements

To compare the simulation and experimental trends, the grown samples are characterized to identify whether the trend of lower voltage with (ln, Ga)N barriers is observed. Figure 7(a) shows the APT reconstruction of the active region of the three-QW LED with (In, Ga)N barriers. The three (In, Ga)N QWs, (Al, Ga)N capping layers, and (In, Ga)N OBs can be clearly observed in this 3D reconstruction. The indium and aluminum concentrations measured in APT are consistent with those expected from growth calibrations. From the profiles, a decrease in the indium fraction at the top side of the (In, Ga)N QB is observed. This thin layer can be explained by unintentional indium desorption from the QB during the growth pause (to allow for the substrate temperature to decrease) before the QW growth. A more uniform indium fraction in the QB could be achieved in future growths by reducing this growth pause.

The six green LEDs are measured under electrical injection to elucidate the impact of alloy quantum barriers on electrical device properties. Consistent with simulations, for all samples, a decrease in forward voltage is observed for (In, Ga)N barriers relative to GaN barriers. The voltage at 20 A cm-2 for all LEDs are shown in Fig. 7(b) and the full J -V curves for representative oneand five-OW LEDs are shown in Fig. 7(c). For both the (In, Ga)N and GaN QB LEDs, Vp first increases from one to three QWs but remains constant from three to five QWs. Previous results on c-plane green LEDs with GaN QBs showed a large voltage increase with increasing OW number due to polarization-related barriers to carrier transport [6]. The moderate increase in voltage with QW number here is attributed to the use of a high period (ln, Ga)N/GaN superlattice and a low aluminum fraction (Al,Ga)N capping layer. LEDs from previous studies that showed a large voltage penalty used a ten-period superlattice and a 20% aluminum cap layer, whereas the structures reported here incorporate a 45-period superlattice and a 4% aluminum cap layer. The high period (In, Ga)N/GaN superlattice leads to the nucleation of inverted hexagonal pyramid defects, known as V-defects [28--31]. The role of V-defects in reducing the QW-QB polarization barriers is supported by recent literature on long-wavelength Ill-nitride LEDs which showed that V-defects may provide a path for carrier injection into the QWs via the semipolar sidewall, thus leading to lower Vp [32-35]. In the present study, the V-defect density is approximately

 2×10^8 cm⁻³, which is below the frequently cited optimal V-defect density value of around 1×10^9 cm⁻³ that leads to substantial improvements in Vp [35]. Therefore, the V-defects are hypothesized to lead to a reduction in the voltage penalty, but the effect would be too small to render the simulation and experimental structures incomparable. Additionally, high aluminum fraction (Al, Ga)N capping layers have been shown to contribute a voltage penalty [16]. The reduced aluminum fraction used here is also expected to result in a lower voltage penalty with each additional QW.

Accounting for the difference in superlattice period and therefore V-defect density, the experimental trend of reduced Vp with (In, Ga)N QBs is consistent with the simulation results. In addition, the peak EL wavelength is blue shifted for LEDs with (In,Ga)N barriers, likely due to the reduced polarization discontinuity at the lower QB/QW interface and therefore reduced QCSE. The EL spectra for the one- and five-QW LEDs with 0% and 4% indium QBs are shown in Fig. 7(d). The peak EL wavelengths for the one-, three-, and five-QW samples with GaN barriers are 505, 515, and 541 nm, respectively. The peak EL wavelengths for the one-, three-, and five-QW samples with (In, Ga)N barriers are 500, 498, and 500 nm, respectively. A blue shift with decreasing QW number for the GaN barrier samples is also observed. This is attributed to an increase in the residual electric field of the p-n junction (due to a decrease in active region width), which cancels out a portion of the polarization-related electric field in the QW. The result is a decrease in the net electric field across the OW and a blue shift as the OCSE is reduced.

IV.CONCLUSION

From our analysis of 3D simulation results, which capture random alloy fluctuations and their associated effects, we find that (In, Ga)N alloy quantum barriers provide several advantages over GaN quantum barriers. Using (In, Ga)N barriers not only reduces the polarization discontinuity at the QB/QW interface, leading to improved modified electron-hole overlap 1Fmoc11² and reduced Vp. but also provides favorable pathways for carriers to inject the QWs. For a single-QW structure with 5% indium in the QB, we observe that regions with higher indium content have higher electron current in the n-side barrier, higher hole current in thep-side barrier, and lower &zz. The high indium fraction regions therefore provide preferential pathways for carrier transport as a result of the lower Z component of the strain-induced piezoelectric polarization. Consistent with the simulation data, LED structures grown by MOCVD with (In, Ga)N quantum barriers also exhibit lower Vp than those with GaN barriers. The findings presented here highlight the role of alloy disorder on carrier transport and overall device behavior as well

as demonstrate the importance of the 3D treatment of III-nitride materials and devices in simulations.

ACKNOWLEDGMENTS

This work was supported by the U.S. Department of Energy under Award No. DE-EE0008204, the National Science Foundation under Grant No. DMS-1839077, grants from the Simons Foundation (Grant No. 601952, J.S. and Grant No. 601954, C.W.), Sandia National Laboratory (Grant No. 2150283), by the Solid State Lighting and Energy Electronic Center (SSLEEC), and by the Taiwanese Ministry of Science and Technology (MOST) under Grant No. MOST 108-2628-E-002-010-MY3. This work was supported by the international collaborative project TECCLON, funded by the French Agence Nationale de la Recherche (ANR), Grant No. ANR-20-CE05-0037-01, and the by the Taiwanese MOST, Grant No. MOST 111-2923-E-002-009. This work made use of the central facilities supported by the NSF MRSEC Program of the NSF under Grant No. DMR 11-21053; a member of the NSF-funded Materials Research Facilities Network. A portion of this work was performed in the UCSB Nanofabrication Facility, an open access laboratory.

- [1] T.-J. Yang, **R.** Shivaraman, J. S. Speck, and Y.-R. Wu, The influence of random indium alloy fluctuations in indium gallium nitride quantum wells on the device behavior, **J.** Appl. Phys. **116**, 113104(2014).
- [2] D. A. Browne, B. Mazumder, Y.-R. Wu, and J. S. Speck, Electron transport in unipolar InGaN/GaN multiple quantum well structures grown by NH3 molecular beam epitaxy, J. Appl. Phys. 117, 185703 (2015).
- [3] W. Hahn, et al., Evidence of Nanoscale Anderson Localization Induced by Intrinsic Compositional Disorder in InGaN/GaN Quantum Wells by Scanning Tunneling Luminescence Spectroscopy, Phys. Rev. B 98, 045305 (2018).
- [4] R. Aleksiejiinas, K. Nomeika, O. Kravcov, S. Nargelas, L. Kuritzky, C. Lynsky, S. Nakamura, C. Weisbuch, and J. S. Speck, Impact of Alloy-Disorder-Induced Localization on Hole Diffusion in Highly Excited c-Plane and m-Plane (ln, Ga)N Quantum Wells, Phys. Rev. Appl. 14, 054043 (2020).
- [5] K. S. Qwah, M. Monavarian, G. Lheureux, J. Wang, Y.-R. Wu, and J. S. Speck, Theoretical and experimental investigations of vertical hole transport through unipolar AIGaN structures: Impacts of random alloy disorder, Appl. Phys. Lett. 117, 022107 (2020).
- [6] C. Lynsky, A. I. Alhassan, G. Lheureux, B. Bonef, S. P. DenBaars, S. Nakamura, Y.-R. Wu, C. Weisbuch, and J. S. Speck, Barriers to Carrier Transport in Multiple Quantum Well Nitride-Based c-Plane Green Light Emitting Diodes, Phys. Rev. Mater. 4, 054604 (2020).
- [7] G. Lheureux, C. Lynsky, Y.-R. Wu, J. S. Speck, and C. Weisbuch, A 3D simulation comparison of carrier transport

- in green and blue c-plane multi-quantum well nitride light emitting diodes, J. Appl. Phys. **128**, 235703 (2020).
- [8] Y.-K. Kuo, J.-Y. Chang, M.-C. Tsai, and S.-H. Yen, Advantages of blue InGaN multiple-quantum well light-emitting diodes with InGaN barriers, Appl. Phys. Lett. 95, Oll 116 (2009).
- [9] J. Xu, et al., Reduction in efficiency droop, forward voltage, ideality factor, and wavelength shift in polarization-matched GalnN/GalnN multi-quantum-well light-emitting diodes, Appl. Phys. Lett. 94, 011113 (2009).
- [10] J. P. Liu, J.-H. Ryou, R. D. Dupuis, J. Han, G. D. Shen, and H. B. Wang, Barrier effect on hole transport and carrier distribution in InGaN/GaN multiple quantum well visible light-emitting diodes, Appl. Phys. Lett. 93, 021102 (2008).
- [11] M. Filoche and S. Mayboroda, Universal mechanism for Anderson and weak localization, PNAS109, 14761 (2012).
- [12] M. Filoche, M. Piccardo, Y.-R. Wu, C.-K. Li, C. Weisbuch, and S. Mayboroda, Localization Landscape Theory of Disorder in Semiconductors. I. Theory and Modeling, Phys. Rev. B95, 144204 (2017).
- [13] D. N. Arnold, G. David, D. Jerison, S. Mayboroda, and M. Filoche, Effective Confining Potential of Quantum States in Disordered Media, Phys. Rev. Lett. 116, 056602 (2016).
- [14] C.-K. Li, M. Piccardo, L.-S. Lu, S. Mayboroda, L. Martinelli, J. Peretti, J. S. Speck, C. Weisbuch, M. Filoche, and Y.-R. Wu, Localization Landscape Theory of Disorder in Semiconductors. III. Application to Carrier Transport and Recombination in Light Emitting Diodes, Phys. Rev. B 95, 144206 (2017).
- [15] Y.-L. Hu, et al., Effect of quantum well cap layer thicknesson the microstructure and performance oflnGaN/GaN solar cells, Appl. Phys. Lett. 100, 161101 (2012).
- [16] T. Shioda, H. Yoshida, K. Tachibana, N. Sugiyama, and S. Nunoue, Enhanced light output power of green LEDs employing AIGaN interlayer in lnGaN/GaN MQW structure onsapphire (000I) substrate, Phys. StatusSolidi A209, 473 (2012).
- [17] A. I. Alhassan, R. M. Farrell, B. Saifaddin, A. Mughal, F. Wu, S. P. DenBaars, S. Nakamura, and J. S. Speck, High luminous efficacy green light-emitting diodes with AlGaN cap layer, Opt. Express 24, 17868 (2016).
- [18] A. I. Alhassan, N. G. Young, R. M. Farrell, C. Pyon, F. Wu, A. Y. Alyamani, S. Nakamura, S. P. DenBaars, and J. S. Speck, Development of high performance green c-plane IIInitride light-emitting diodes, Opt. Express 26, 5591 (2018).
- [19] B. Bonef, M. Catalano, C. Lund, S. P. Denbaars, S. Nakamura, U. K. Mishra, M. J. Kim, and S. Keller, Indium segregation in a-polar InGaN quantum wells evidenced by energy dispersive x-ray spectroscopy and atom probe tomography, Appl. Phys. Lett. 110, 14310I (2017).
- [20] C. Geuzaine and J.-F. Remade, Gmsh: A three-dimensional finite element mesh generator with built-in pre- and postprocessing facilities, Int. J. Nurner. Methods Eng. 79, 1309 (2009).
- [2 I] See http://gmsh.info/ for more information about GMSH, a three-dimensional finite element mesh generator.
- [22] Y.-R. Wu, R. Shivaraman, K.-C. Wang, and J. S. Speck, Analyzing the physical properties oflnGaN multiple quantum well light emitting diodes from nano scale structure, Appl. Phys. Lett. tot, 083505 (2012).

- [23] C.-K. Wu, C.-K. Li, and Y.-R. Wu, Percolation transport study in nitride based LED by considering the random alloy fluctuation, J. Comput. Electron. 14,416 (2015).
- [24] See http://yrwu-wk.ee.ntu.edu.tw/ for "Optoelectronic device simulation laboratory".
- [25] A. E. Romanov, T. J. Baker, S. Nakamura, and J. S. Speck, Strain-induced polarization in wurtzite III-nitride semipolar layers, J. Appl. Phys. 100, 023522 (2006).
- [26] V.Fiorentini, F. Bernardini, and 0. Ambacher, Evidence for nonlinear macroscopic polarization in III-V nitride alloy heterostructures, Appl. Phys. Lett. 80, 1204 (2002).
- [27] O. Ambacher, et al., Pyroelectric Properties of Al(ln)GaN/ GaN Hetero- and quantum well structures, J. Phys.: Condens. Matter 14, 3399 (2002).
- [28] B. Heying, E. J. Tarsa, C.R. Elsass, P. Fini, S. P. DenBaars, and J. S. Speck, Dislocation mediated surface morphology ofGaN, J. Appl. Phys. 85, 6470 (1999).
- [29] X. H. Wu, C. R. Elsass, A. Abare, M. Mack, S. Keller, P. M. Petroff, S. P. DenBaars, J. S. Speck, and S. J. Rosner, Structural origin of V-defects and correlation with localized excitonic centers in lnGaN/GaN multiple quantum wells, Appl. Phys. Lett. 72, 692 (1998).

- [30] **M.** Shiojiri, C. C. Chuo, J. T. Hsu, J. R. Yang, and H. Saijo, Structure and formation mechanism of V defects in multiple lnGaN/GaN quantum well layers, **J.** Appl. Phys. 99, 073505 (2006).
- [31] 1.-H. Kim, H.-S. Park, Y.-J. Park, and T. Kim, Formation of V-shaped pits in InGaN/GaN multiquantum wells and bulk InGaN films, Appl. Phys. Lett. 73, 1634 (1998).
- [32] Z. Quan, L. Wang, C. Zheng, J. Liu, and F. Jiang, Roles of V-Shaped pitson the improvement of quantum efficiency in lnGaN/GaN multiple quantum well light-emitting diodes, J. Appl. Phys. 116, 183107 (2014).
- [33] C.-K. Li, C.-K. Wu, C.-C. Hsu, L.-S. Lu, H. Li, T.-C. Lu, and Y.-R. Wu, 3D numerical modeling of the carrier transport and radiative efficiency for lnGaN/GaN light emitting diodes with V-shaped pits, AIP Adv. 6, 055208 (2016).
- [34] F. Jiang, et al., Efficient lnGaN-based yellow-light-emitting diodes, Photonics Res. 7, 144 (2019).
- [35] S. Zhang, et al., Efficient emission of lnGaN-based lightemitting diodes: Toward orange and red, Photonics Res. 8, 1671 (2020).